Available online at www.sciencedirect.com
ScienceDirect
Computers & Fluids 35 (2006) 1239–1251
computers & fluids
www.elsevier.com/locate/compfluid

Application of spectral forcing in lattice-Boltzmann simulations of homogeneous turbulence

A. ten Cate [a], E. van Vliet [b], J.J. Derksen [c,*], H.E.A. Van den Akker [c]

[a] Department of Chemical Engineering, Princeton University, Princeton, NJ 08544, USA
[b] Department of Chemical Engineering, Iowa State University, Ames, IA 50011, USA
[c] Kramers Laboratorium voor Fysische Technologie, Prins Bernhardlaan 6, 2628 BW Delft, The Netherlands

Received 20 July 2004; received in revised form 22 March 2005; accepted 20 June 2005
Available online 19 August 2005

Abstract

An efficient numerical method for the direct simulation of homogeneous turbulent flow has been obtained by combining a spectral forcing algorithm for homogeneous turbulence with a lattice-Boltzmann scheme for solution of the continuity and Navier–Stokes equations. The spectral forcing scheme of Alvelius [Alvelius K. Random forcing of three-dimensional homogeneous turbulence. Phys Fluids 1999;11(7):1880–89] is used which allows control of the power input by eliminating the force–velocity correlation in the Fourier domain and enables anisotropic forcing. A priori chosen properties such as the Kolmogorov length scale, the integral length scale and the integral time scale are recovered. This demonstrates that the scheme works accurately with the lattice-Boltzmann method and that all specific features of the forcing scheme are recovered in the lattice-Boltzmann implementation.

1. Introduction

A well-known characteristic of turbulent flows is that energy production occurs at large length scales ($\mathcal{O}(\Lambda)$, the integral length scale), which are typically associated with the largest dimensions of the flow field, while the dissipation of kinetic energy occurs at smaller length scales, characterised by the Kolmogorov scale ($\mathcal{O}(\eta)$). A typical energy spectrum of a turbulent flow is given in Fig. 1. The maximum in the energy spectrum is found at the large scales, that is, at small wave numbers. Energy is transferred from large to small length scales and this transfer process is characterised by the well-known universal power-law spectrum [2]

$$E(k) = c_K \epsilon^{2/3} k^{-5/3}. \quad (1)$$

At the smallest scales the kinetic energy is dissipated rapidly and the energy spectrum decays steeply towards zero. One classical concept used in the interpretation of turbulence is the separation of scales. At large scales the structure of the turbulent flow holds a relation to the structure of the energy source (e.g. the shape of an impeller or vessel or the wing of an airplane) and can be highly anisotropic. Towards smaller length scales the structure of the turbulent flow loses its relation to the macroscopic structures and tends to isotropy and homogeneity.

The main issue in numerical simulations of turbulent flows is that the large and the small scales may differ by orders of magnitude. Consequently, for accurate computation of all length scales present in a turbulent flow, typically very high resolution is required, resulting in very large computational domains which is generally not feasible.

Turbulence modeling uses the universality of turbulence in modeling the dissipative behaviour of the turbulent flow. For example, in large eddy simulations (LES)

* Corresponding author. Tel.: +31 15 2787968; fax: +31 15 2782838.
E-mail address: jos@klft.tn.tudelft.nl (J.J. Derksen).

0045-7930/$ - see front matter © 2005 Elsevier Ltd. All rights reserved.
doi:10.1016/j.compfluid.2005.06.001

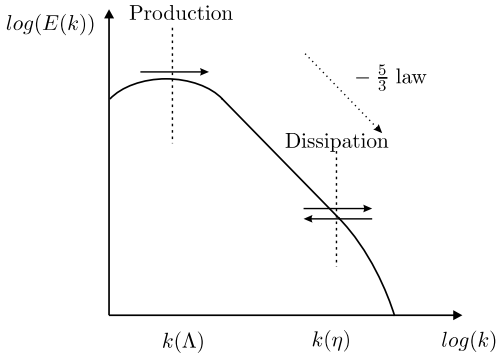

Fig. 1. Typical power spectrum of the kinetic energy in turbulent flow.

the flow field is usually simulated at a coarse grid that captures the large structures in the flow field. The influence of the turbulent fluid motion at sub-grid length scales is then modeled as a local turbulent viscosity that is determined from the local rate of deformation of the resolved scales [3,4].

A different perspective in studying turbulent flow is to model the behaviour of the fluid motion at the *large* length scales and simulate the flow field up to the smallest length scales. For this approach, an artificial fluctuating body force is defined that sets the fluid in motion at the largest length scales. This force mimics a homogeneous source of energy that enters the flow field at a large length scale. By solving the Navier–Stokes equations while ensuring that all scales of the flow field up to the smallest length scales are resolved, the microscopic scales will evolve naturally.

For simulation of forced turbulent flows different types of forcing schemes have been developed. Typical examples are the schemes of Eswaran and Pope [5], and more recently those of Overholt and Pope [6] or Alvelius [1]. In these approaches, a body force is defined at low wave numbers and imposed on the flow field. Direct simulation of forced turbulent flows still requires a separation of length scales between the production and dissipation scales and large computational domains are needed. For this purpose, there is clearly a need for efficient numerical schemes for solution of the Navier–Stokes equations.

Generally, spectral forcing is combined with a pseudo-spectral method for numerical solution of the Navier–Stokes equations. Pseudo-spectral methods provide a natural choice for simulation of forced turbulence since with this type of schemes the Navier–Stokes equations are solved (at least partially) in wave number space. Introducing spectral forcing to the flow field is then straightforward since both methods are defined in the Fourier domain. However, the application of spectral forcing in numerical simulations of turbulent flows is not limited to pseudo-spectral methods.

The objective of this paper is to demonstrate that the lattice-Boltzmann method provides a good alternative as a numerical method for direct simulation of forced isotropic turbulence. In the lattice-Boltzmann method the fluid motion is described at a microscopic level in terms of fluid masses that propagate on an equidistant grid at discrete time steps. At the level of the continuum equations the lattice-Boltzmann method provides an efficient, accurate and stable numerical scheme to solve the Navier–Stokes equations [7–10]. The lattice-Boltzmann method allows for local application of body forces and hence the method can be combined with a spectral forcing algorithm in the direct simulation of forced turbulent flows. For the simulations presented in this paper the lattice-Boltzmann scheme of Eggels and Somers [11] was used.

One typical requirement of the lattice-Boltzmann method is that fluid velocities are much smaller than the speed of sound of the scheme. Therefore, we use the forcing method of Alvelius [1] in this paper. This method offers the possibility to reduce uncontrolled velocity fluctuations that occur in forced turbulence due to force–velocity correlation. Another advantageous feature of this forcing scheme is that it offers the possibility to generate axisymmetric anisotropic turbulence.

The outline of this paper is the following. In Section 2, the theoretical background and the description of the forcing method is briefly reproduced. In Section 3, the lattice-Boltzmann scheme is introduced and details on implementation of the forcing scheme are discussed. In Section 4, simulation settings are presented that test specific features of the forcing method; quality of the statistical quantities of the turbulent flow field, controlling the force–velocity correlation, numerical stability at excessively large Reynolds numbers, the isotropy of the flow field and, anisotropic forcing. In Section 5, the results are discussed and finally, in Section 6, conclusions are presented.

2. Spectral forcing

In this section, the forcing method developed by Alvelius [1] is presented. The body force that drives the flow field is defined in wave number space. The random force is active in a spherical shell at small wave numbers where the forcing intensity is given by a prescribed distribution over the wave numbers. Alvelius [1] recognised that for such a force, the power input in the Navier–Stokes equations contains two contributions. Consider the force to be constant for the duration of one time step. The discretised power input for the duration of one time step Δt (i.e. $n \to n+1$) becomes

$$\frac{K^{n+1}-K^n}{\Delta t} = \frac{1}{2}\overline{f_\alpha^n f_\alpha^n}\Delta t + \overline{u_\alpha^n f_\alpha^n} = P_1 + P_2, \tag{2}$$

where the overbar indicates the spatial average and the summation convention is implied on repeated Greek

subscripts. Thus, P_1 gives the constant power input due to the force–force correlation, while P_2 represents an uncontrolled fluctuating quantity due to force–velocity correlation. As will be demonstrated, the force can be chosen in such a way that (by construction) the term P_2 is set to zero at each time step.

The random force is chosen to be divergence free to prevent that it directly influences the pressure. In Fourier[1] space this implies:

$$k_\alpha \hat{f}_\alpha = 0, \tag{3}$$

which is obeyed by choosing

$$\hat{f}_\alpha(\mathbf{k},t) = A_{\text{ran}}(\mathbf{k},t)e_{1\alpha}(\mathbf{k}) + B_{\text{ran}}(\mathbf{k},t)e_{2\alpha}(\mathbf{k}), \tag{4}$$

where $\mathbf{e}_1$ and $\mathbf{e}_2$ are two orthogonal unit vectors, normal to $\mathbf{k}$. A_{ran} and B_{ran} are terms that distribute the power input randomly in the directions $\mathbf{e}_1$ and $\mathbf{e}_2$. Alvelius' [1] choice for the unit vectors $\mathbf{e}_1$ and $\mathbf{e}_2$ was

$$e_{1x} = \frac{k_y}{(k_x^2+k_y^2)^{1/2}}; \quad e_{1y} = -\frac{k_x}{(k_x^2+k_y^2)^{1/2}}; \quad e_{1z} = 0, \tag{5}$$

and

$$e_{2x} = \frac{k_x k_z}{k(k_x^2+k_y^2)^{1/2}}; \quad e_{2y} = \frac{k_y k_z}{k(k_x^2+k_y^2)^{1/2}}; \quad e_{2z} = -\frac{(k_x^2+k_y^2)^{1/2}}{k}, \tag{6}$$

where $k = |\mathbf{k}|$.

The power input of the force–force correlation in wave number space is given by

$$\frac{P_1}{\Delta t} = \frac{1}{2}\overline{f_\alpha^n f_\alpha^n} = 2\pi \int_0^\infty k^2 \langle \hat{f}_\alpha \hat{f}_\alpha^* \rangle \, \mathrm{d}k \equiv \int_0^\infty F(k)\,\mathrm{d}k, \tag{7}$$

where $F(k)$ is the function that defines the distribution of the forcing spectrum in wave number space (* indicates the complex conjugate). The form for A_{ran} and B_{ran} was chosen as

$$A_{\text{ran}} = \left(\frac{F(k)}{2\pi k^2}\right)^{1/2} \exp(\mathrm{i}\theta_1) g_{\text{A}}(\phi), \tag{8}$$

$$B_{\text{ran}} = \left(\frac{F(k)}{2\pi k^2}\right)^{1/2} \exp(\mathrm{i}\theta_2) g_{\text{B}}(\phi), \tag{9}$$

where g_{A} and g_{B} are random factors that determine the direction of the forcing vector at each wave number and that obey $g_{\text{A}}^2 + g_{\text{B}}^2 = 1$. An appropriate choice for the functions g_{A} and g_{B}, that vary with the angle ϕ, is given below. Both $\phi \in [0, \pi]$, and $\theta_1, \theta_2 \in [0, 2\pi]$ are chosen as uniformly distributed random numbers and selected each time step for each discrete wave number.

The distribution of the power input over the wave numbers is determined by the definition of $F(k)$. In order to determine the power input a priori, a Gaussian distribution of the spectrum function $F(k)$ is chosen, which is schematically represented in Fig. 2. The force distribution is active in the wave number range $k \in [k_{\text{a}}, k_{\text{b}}]$, with a forcing maximum at k_{f},

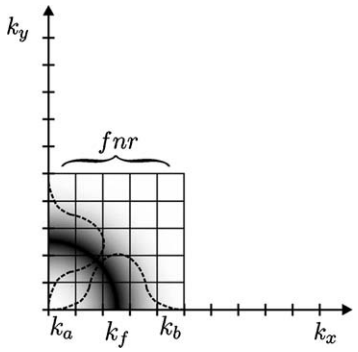

Fig. 2. 2D representation of the placement of the forcing distribution in the Fourier domain. The dotted curves indicate the placement of the Gaussian distribution of the force signal along the x and y axis, the grey scale contour indicates the position of the Gaussian distribution in the 2D plane.

$$F(k) = A \exp\left(-\frac{(k-k_{\text{f}})^2}{c}\right), \tag{10}$$

and where c is a parameter that determines the width of the distribution. The power input is determined by the amplitude A according to

$$A = \frac{P_1}{\Delta t} \frac{1}{\int_{k_{\text{a}}}^{k_{\text{b}}} \exp\left(-\frac{(k-k_{\text{f}})^2}{c}\right) \mathrm{d}k}. \tag{11}$$

To control the power input, a condition needs to be determined for P_2 to remain zero each time step. The force–velocity correlation is given by

$$P_2 = \overline{\hat{u}_\alpha^n \hat{f}_\alpha^n} = \int\int\int_{k_V} \hat{u}_\alpha(\mathbf{k},t)\hat{f}_\alpha^*(\mathbf{k},t)\,\mathrm{d}k_x\,\mathrm{d}k_y\,\mathrm{d}k_z, \tag{12}$$

which is generally non-zero on the interval $[k_{\text{a}}, k_{\text{b}}]$ and is zero by definition outside this range. P_2 is set to zero by making $\hat{u}_\alpha(\mathbf{k},t)\hat{f}_\alpha^*(\mathbf{k},t) = 0$ at each of the active wave numbers. This gives the condition:

$$\text{Real}[A_{\text{ran}}^* \xi_1 + B_{\text{ran}}^* \xi_2] = 0, \tag{13}$$

with $\xi_1 = \hat{u}_\alpha e_{1\alpha}$ and $\xi_2 = \hat{u}_\alpha e_{2\alpha}$. Using this constraint, Eqs. (8) and (9) lose one degree of freedom and θ_1 can be determined from

$$\tan\theta_1 = \frac{g_{\text{A}}(\phi)\text{Real}[\xi_1] + g_{\text{B}}(\phi)(\sin\psi\text{Imag}[\xi_2] + \cos\psi\text{Real}[\xi_2])}{-g_{\text{A}}(\phi)\text{Imag}[\xi_1] + g_{\text{B}}(\phi)(\sin\psi\text{Real}[\xi_2] - \cos\psi\text{Imag}[\xi_2])}, \tag{14}$$

after choosing randomly for each wave number at each time step the angle ψ, which is defined as $\psi = \theta_2 - \theta_1$, on the interval $[0, 2\pi]$.

[1] Superscript ˆ indicates the Fourier transform of a variable.

A choice for the functions g_A and g_B needs to be made to determine the mean orientation of the power input. This is determined by the product of $g_A e_{1\alpha}$ and the product of $g_B e_{2\alpha}$. With the choice for the e-vectors of Eqs. (5) and (6), the power input specified for the different directions becomes,

$$\langle P_x \rangle = \langle P_y \rangle = P_1 \left(\frac{1}{6} + \frac{1}{3} \langle g_A^2 \rangle \right), \tag{15}$$

$$\langle P_z \rangle = P_1 \frac{2}{3} (1 - \langle g_A^2 \rangle), \tag{16}$$

and the ratio of the power input, r_f, in the different x–z or y–z direction becomes

$$r_f = \frac{\langle P_x \rangle}{\langle P_z \rangle} = \frac{1 + 2\langle g_A^2 \rangle}{4(1 - \langle g_A^2 \rangle)}, \tag{17}$$

which is determined by the choice of $g_A(\phi)$. By choosing $g_A = \sin(2\phi)$, $g_B = \cos(2\phi)$, $r_f = 1$, i.e. the forcing is isotropic. Choosing g_A in the form

$$g_A(\phi) = -\frac{\tanh(b(\phi - \pi/2))}{\tanh(b\pi/2)}, \tag{18}$$

results in

$$\langle g_A^2(\phi) \rangle = \frac{1}{\tanh(b\pi/2)} \left(\frac{1}{\tanh(b\pi/2)} - \frac{2}{b\pi} \right), \tag{19}$$

where b determines the degree of anisotropy. With our choice of e-vectors (Eqs. (5) and (6)), axisymmetric anisotropic turbulence is obtained.

3. Implementation of spectral forcing

3.1. The lattice-Boltzmann method

In recent years the lattice-Boltzmann method has received much attention for simulation of fluid flow. A main advantage of the method is that it is a second order accurate numerical scheme of which the numerical operations are practically local and only involve minimal near-neighbour interactions. Application of this method on distributed parallel computer platforms is therefore highly efficient. For the direct simulation of turbulent flows, this feature is very desirable because large domains, i.e. large computer memory and long computational time, are required.

The principle of the lattice-Boltzmann method is essentially based on mimicking the collision process of the molecules of a kinetic gas on a discrete grid. The fluid is represented by masses that propagate on a discrete grid at discrete time steps. The grid is a regular cubic lattice with grid node locations $\mathbf{x}$ and equidistant grid spacing Δx. The fluid masses, $n_i(\mathbf{x}, t)$, are located on the grid nodes and are distributed over $i = 0, 1, \ldots, M$ directions of the discrete grid. At each discrete time step, the masses propagate to their neighbour nodes in the discrete i directions with fixed velocities $c_{i\alpha}$. The incoming masses collide, i.e. exchange momentum. The lattice-Boltzmann equation (LBE) is the discretised evolution equation of this process, given by

$$n_i(\mathbf{x} + c_{i\alpha}\Delta t, t + \Delta t) = n_i(\mathbf{x}, t) + \Omega_i(\mathbf{x}, t). \tag{20}$$

The fluid density and momentum are defined as

$$\rho(\mathbf{x}, t) = \sum_M n_i(\mathbf{x}, t) \quad \rho u_\alpha(\mathbf{x}, t) = \sum_M n_i(\mathbf{x}, t) c_{i\alpha}, \tag{21}$$

while the collision operator is defined such that mass and momentum are conserved,

$$\sum_M \Omega_i(\mathbf{x}, t) = 0 \qquad \sum_M \Omega_i(\mathbf{x}, t) c_{i\alpha} = \rho f_\alpha(\mathbf{x}, t), \tag{22}$$

where the force f_α is the homogeneous body force that acts locally on the fluid. In the case of forced isotropic turbulence this force is the term that is computed via the spectral forcing method.

The essence of the lattice-Boltzmann scheme is captured in the formulation and computation of the collision operator. Generally, the collision process is modeled via the BGK [12] collision operator. The collision process is driven by a relaxation of the distribution of mass n_i to an equilibrium state

$$\Omega_i(\mathbf{x}, t) = -\frac{1}{\tau}(n_i(\mathbf{x}, t) - n_i^{\mathrm{eq}}(\mathbf{x}, t)) + \Delta t F_i(\mathbf{x}, t), \tag{23}$$

where n_i^{eq} is the equilibrium distribution, given as

$$n_i^{\mathrm{eq}}(\mathbf{x}, t) = \omega_i \left[1 + \frac{c_{i\alpha} u_\alpha}{c_s^2} + \frac{u_\alpha u_\beta \{c_{i\alpha} c_{i\beta} - \delta_{\alpha\beta}\}}{2c_s^4} \right], \tag{24}$$

which is again fully local, since the equilibrium distribution is computed based on the local velocity and density. In the equilibrium distribution the parameter c_s is the speed of sound of the lattice-Boltzmann scheme and ω_i is a weight factor. Specific choices of these parameters are made based on the number of dimensions and number of discrete directions M, and are usually indicated as [13] D2Q9, for the 2D 9 speed model, while in 3D variations such as the D3Q15, D3Q18 and D3Q19 speed model exist.

Viscosity is introduced via the relaxation process. It can be shown that the above set of equations approximates the continuity

$$\frac{\partial \rho}{\partial t} + \frac{\partial \rho u_\alpha}{\partial x_\alpha} = 0, \tag{25}$$

and Navier–Stokes equations for incompressible fluid flow

$$\frac{\partial \rho u_\alpha}{\partial t} + \frac{\partial \rho u_\alpha u_\beta}{\partial x_\beta} = -\frac{\partial p}{\partial x_\alpha} + \frac{\partial}{\partial x_\beta} \left[\nu \rho \left(\frac{\partial u_\beta}{\partial x_\alpha} + \frac{\partial \rho u_\alpha}{\partial x_\beta} \right) \right] + \rho f_\alpha, \tag{26}$$

in the limit of low Mach numbers, i.e. for $|u_\alpha| \ll c_s$. Here p indicates the fluid pressure. The kinematic viscosity ν and relaxation parameter τ are related as

$$\nu = c_s^2\left(\tau - \frac{1}{2}\right)\Delta t. \tag{27}$$

For the application of an inhomogeneous body force in the lattice-Boltzmann scheme, the force term $F_i(\mathbf{x},t)$ needs to be defined. A straightforward choice is to define the force as

$$F_i(\mathbf{x},t) = \omega_i \frac{c_{i\alpha} f_\alpha(\mathbf{x},t)\rho(\mathbf{x},t)}{c_s^2}. \tag{28}$$

The paper of Guo et al. [14] gives a discussion on the accuracy of this force term. Generally, to prevent the formation of artifacts in the velocity field, it is advised to use an adjusted formulation of the force term to remove possible artifacts. However, in the case of turbulent forcing, the occurrence of artefacts is negligible since these are proportional to $\nabla_\alpha f_{i\alpha}$. Since the unsteady body force is defined on large length scales, the spatial derivatives of the body force term become negligibly small.

3.2. Numerical implementation

For the simulations presented in this paper, a specific form of the D3Q18 lattice-Boltzmann scheme was used, as given by Eggels and Somers [11,15]. In this scheme the speed of sound is $c_s = \sqrt{\frac{1}{2}}\Delta x/\Delta t$. The grid spacing Δx and time step Δt were chosen as unity and all quantities are further expressed in lattice units, $1\ \mathrm{lu} \equiv 1\ \Delta x$ and time steps $1\ \mathrm{ts} \equiv 1\Delta t$. This scheme contains additional damping of higher-order terms that are present in the lattice-Boltzmann scheme. The main advantage of this scheme as compared to the regular BGK scheme is that it possesses improved numerical stability for simulations at very low viscosities. This is, however, not a restriction for the use of turbulent forcing in the lattice-Boltzmann scheme, since we also tested the forcing scheme successfully in a BGK D3Q19 scheme (not further reported here).

The forcing scheme presented in the previous section is used to compute the force field $\hat{f}_\alpha(\mathbf{k},t)$ in Fourier space. Since the lattice-Boltzmann method is defined in physical space, the force must be transformed to the physical domain before being applied. This is achieved via an inverse Fourier transform, after which the force is straightforwardly imposed. Implementation of the controlled version of the forcing scheme requires the Fourier transform of the velocity field, $\hat{u}_\alpha(\mathbf{k},t)$. As a result, application of the forcing scheme in three-dimensions requires three inverse Fourier transforms for the generation of the force field, while the controlled version of the forcing scheme requires an additional three forward Fourier transforms of the velocity field.

For efficient numerical simulation the lattice-Boltzmann scheme was implemented in a parallelized code using MPI. For the 3D Fourier transform the MPI-enabled version 2.1.5 of the FFTW fast Fourier transform library [16] was used. To reduce memory usage and improve computational performance, the FFT's were transformed in-place and in transposed order. The MPI parallel version of the fast Fourier transform can only be computed in a slab-wise domain decomposition of the field that is to be transformed. Therefore, the lattice-Boltzmann code was parallelized via slab-wise domain decomposition in the x-direction.

4. Simulations

The conditions of the simulations are defined by three parameters; the length $l*$, which defines the large turbulence scales, the characteristic velocity $u*$, through which the time scale of the simulation is fixed, and the Kolmogorov scale η, which determines the smallest scales in the simulation and consequently determines the turbulent Reynolds number.

The forcing length scale is defined as $l* = 2\pi/k_f$, with k_f the wave number of maximum forcing amplitude (see also Fig. 2). The forcing wave number is determined via the domain size $nx \times ny \times nz$ grid points. In all simulations presented in this paper, the domain is cubic and nx, ny and nz are equal. The forcing is defined on the wave number interval $[k_a, k_b]$ by the number of discrete Fourier modes in this interval, indicated by f_{nr}. The smallest wave number that can be represented on the grid corresponds to the domain size as $k_0 = k_a = 2\pi/nx$. The discrete wave numbers in the Fourier domain are integer multiplications of k_0. The largest wave number to which forcing is applied is determined as $k_b = f_{nr} \times k_a$, while the forcing maximum is chosen as the central value in the range $[k_a, k_b]$.

The velocity $u*$ represents a characteristic velocity of the turbulent flow. This characteristic velocity is chosen typically one order of magnitude smaller than the speed of sound c_s to assure that the simulations obey the incompressibility restriction. The velocity $u*$ is used as a way to determine the power input via the scaling law for energy dissipation $\epsilon \simeq \mathscr{U}^3/\mathscr{L}$ and the assumption that statistical equilibrium is achieved between dissipation and production, $\epsilon = P$. Thus, by defining the length scale $l*$ and the velocity $u*$ the power input is set as $P = u*^3/l*$ (used as input in Eq. (11)).

The third parameter is the Kolmogorov length scale η. This length scale is a measure for the smallest distance over which gradients in the flow field can exist. In terms of lattice-Boltzmann units, a Kolmogorov length of 1 [lu] corresponds to one grid spacing. In spectral simulations, the resolution is often defined in terms of $k_{max} \times \eta$ where k_{max} is the largest resolved wave number, which is

given by $k_{max} = nx/2 \times k_0 = \pi$. A criterion for proper resolution of a DNS of turbulent flow is given by $k_{max} \times \eta > 1$ [17]. Accordingly, the Kolmogorov length scale should obey $\eta > 0.318$ [lu]. Choosing η fixes the kinematic viscosity of the fluid via the definition of the Kolmogorov length and the equilibrium assumption between production and dissipation; $\nu = (P\eta^4)^{1/3}$.

With the definition of $l*$, $u*$ and the viscosity, a forcing Reynolds number is obtained that fully characterises the simulation conditions,

$$Re_{force} = \frac{u* \, l*}{\nu} = \left(\frac{l*}{\eta}\right)^{4/3}. \tag{29}$$

The parameter settings of the simulations discussed in this paper are given in Table 1. A number of parameters were identical for simulations F_1–F_7. The domain size was $nx \times ny \times nz \sim 128^3$ and $u* = 0.05$ [lu/ts]. The simulations were executed for 15,000 [ts], corresponding to 11.7 forcing time scales $l*/u*$ for simulation F_5 and 23.4 $l*/u*$ for the other simulations. All simulations have controlled power input unless stated differently. In all simulations presented in this paper the concentration parameter c that appears in Eq. (10) was chosen as 1.0. This value was chosen such that the Gaussian distribution of the force spectrum becomes rather wide and the power input becomes distributed over all the discrete wave numbers on the interval $[k_a, k_b]$. In the work of Alvelius [1], this parameter is chosen much smaller, as 0.01. Such a small parameter practically focuses the power input on a single wave number, rather than distributing the power input over the interval $[k_a, k_b]$.

In simulations F_1 and F_2, the implementation of the forcing scheme into the lattice-Boltzmann scheme is demonstrated and the difference between controlled and uncontrolled forcing is tested. In cases F_3, F_1 and F_4, the forcing Reynolds number is varied in increasing order to investigate the influence of a decreasing Kolmogorov length scale, such that it violates the limit for a well resolved direct simulation. The resolution-constraint $k_{max}\eta > 1$ is violated to observe its impact on the numerical stability and physical validity of the simulations. In simulation F_5, the impact of the number of forcing Fourier modes on the flow field is investigated. In simulation F_6 forcing conditions were imposed using a set of 120 force fields $f_\alpha(\mathbf{x}, t)$. These fields were prepared and stored prior to execution of the simulation, to increase the computational speed. As a result, the white noise forcing signal is mimicked by a limited set of force field realisations. The resulting flow field and time series are compared with simulations F_1 and F_2. Finally, run F_7 was carried out to test the feature of anisotropic forcing in the lattice-Boltzmann simulations.

5. Results and discussion

5.1. Statistical quantities

Dimensionless statistical quantities that characterise the turbulent flow are given in Table 2.

To characterise the large scales of the turbulent flow, an integral length scale Λ is given. This scale is determined both via the scaling law $\Lambda = u'^3/\epsilon$ (u' is the rms fluid velocity) and via the energy spectrum,

$$\Lambda_s = \frac{\pi}{2u'^2} \int_0^{k_{max}} \frac{E(k)}{k} \, dk. \tag{30}$$

These two integral scales have a different physical meaning. The integral scale Λ represents the large scale of the flow field based on the energy dissipation whereas Λ_s is a measure for the distance over which the velocity correlation drops to zero [18]. Λ_s depends on the spatial structure of the flow field, which is determined by the size of the computational grid and the spectral forcing.

A Reynolds number based on the Taylor micro-scale is often used to characterise simulations of forced isotropic turbulence. The Taylor micro-scale is given by

$$\lambda = \left(\frac{15\nu u'^2}{\epsilon}\right)^{1/2}. \tag{31}$$

The table shows that the Taylor Reynolds number is about one order of magnitude smaller than the forcing Reynolds number. It is also noticed that Re_λ is practically constant for simulations with the same forcing Reynolds number.

Table 1
Parameter settings of forced turbulence simulations F_1 to F_7

Run	η [lu]	$k_{max}\eta$ [–]	f_{nr} [–]	$l*$ [lu]	Re_{force} [–]	Remark
F_1	0.5	1.571	7	32	256	
F_2	0.5	1.571	7	32	256	Uncontrolled
F_3	1	3.142	7	32	102	
F_4	0.1	0.314	7	32	2189	
F_5	1	3.142	3	64	256	
F_6	0.5	1.571	7	32	256	Force from file
F_7	1	3.142	7	32	102	Anisotropic, $b = 10$

Table 2
Simulation results

Run	$k_{max}\eta$	Re_λ	$u'*$	$\Lambda*$	Λ_s*	T_0*	$(\epsilon/P)_{lB}$	$(\epsilon/P)_s$	S_g
F_1	1.56	39.8	0.80	0.51	0.34	0.42	1.02	0.95	−0.40
F_2	1.56	39.9	0.81	0.51	0.34	0.43	1.02	0.94	−0.40
F_3	3.14	19.9	0.72	0.36	0.40	0.55	1.01	1.00	−0.43
F_4	0.36	171.6	0.86	1.05	0.28	0.32	0.60	0.41	−0.18
F_5	3.02	41.7	0.85	0.53	0.33	0.38	1.17	1.21	−0.38
F_6	1.58	39.4	0.79	0.51	0.34	0.43	0.98	0.93	−0.41
F_7	3.12	25.2	0.81	0.51	0.34	0.42	1.02	0.96	−0.40

Properties indicated with $a*$ were non-dimensionalised with $u*$ and $l*$.

The integral time scale given in the table is associated with the motion of the large scales in the fluid flow, and is defined by

$$T_0 = \Lambda_s/u'. \tag{32}$$

Two properties given in the table that are directly linked to the resolution of the small scales in the flow field are the rate of energy dissipation,

$$\epsilon \equiv \nu\overline{\left(\frac{\partial u_i}{\partial x_j}+\frac{\partial u_j}{\partial x_i}\right)\frac{\partial u_j}{\partial x_i}} \equiv \int_0^{k_{\max}} D(k)\,\mathrm{d}k \equiv 2\nu\int_0^{k_{\max}} k^2E(k)\,\mathrm{d}k, \tag{33}$$

and the velocity derivative skewness,

$$S_g = \frac{\left\langle\left(\frac{\partial u}{\partial x}\right)^3\right\rangle}{\left\langle\left(\frac{\partial u}{\partial x}\right)^2\right\rangle^{3/2}}. \tag{34}$$

With an increasing turbulent Reynolds number the small structures in the flow field become smaller. In a DNS, the smallest length scales still have to be captured accurately on the computational grid. Both the rate of energy dissipation and the velocity derivative skewness give an indication of the accurate representation of the velocity gradients and give an indication of the quality of the simulations.

The rate of energy dissipation can be determined along two routes for a turbulent flow. It can be determined via the rate of deformation of the flow field, or it can be determined from the energy spectrum (Eq. (33)). In Table 2, the values of the rate of energy dissipation as obtained along both routes are presented (ϵ_{lB} from the lattice-Boltzmann scheme and ϵ_s via the energy spectrum), as a consistency check of the lattice-Boltzmann scheme. The lattice-Boltzmann scheme inherently contains the deformation rate of the flow field [11], from which the rate of energy dissipation can be computed directly, i.e. without the need to determine spatial derivatives from the velocity field via a difference scheme.

In steady turbulent flows, the rate of energy dissipation and the power input should be in statistical equilibrium, and the ratio of power input over energy dissipation should be 1. Table 2 shows that ϵ_s as well as ϵ_{lB} generally are in good agreement, which demonstrates that the velocity field and the gradients are calculated in a consistent manner. Apart from simulation F_4, where the resolution is violated, the ratios ϵ/P are close to 1.0. The somewhat lower rate of energy dissipation obtained via the energy spectrum may be a result of the discretisation of the 1D energy spectrum as obtained from the 3D velocity field.

In simulation F_4, the Kolmogorov length scale was set to 0.1 grid spacing. This violates the rule of thumb for accurate DNS. The rate of energy dissipation obtained from the simulations indicates that only 60% of the power input is recovered, and the small scales of the flow field are not captured accurately by the simulations. This will be further discussed in a later section.

The velocity derivative skewness S_g is the normalized third order moment of the distribution of the velocity gradients, and can be associated with the time evolution of the longitudinal velocity correlation functions [19,18]. It is a measure for the shape of the pdf of the velocity gradients. This parameter obtains a negative value which varies with the Reynolds number, and for DNS simulations is reported in the range -0.4 to -0.5 for both decaying and sustained isotropic turbulence (e.g. [1,20]). The values in the table indicate that for well resolved turbulent conditions a value is observed in the same range, whereas for simulation F_4, the reported value is found to be significantly larger.

5.2. Transient behaviour

A comparison of the evolution of the kinetic energy and the rate of energy dissipation of simulations F_1, F_2 and F_6 is given in Fig. 3. This figure shows the difference between controlled and uncontrolled forcing and the influence of forcing while using a true white noise forcing signal compared to a signal generated by using a limited number of forcing fields. At the start of the simulations the fluid was at rest. The initial slope of the simulations should therefore be equal to the power input P, since in the absence of dissipation, $\mathrm{d}K/\mathrm{d}t = P$ holds. This is indicated by the tangent line through the origin of the time series.

Fig. 3(c) shows that the initial slope of the kinetic energy is below the expected value while for the two other cases the initial energy increase has the expected behaviour. Using a limited number of force fields (F_6) results in a reduced power input. This is clear from the time series and from the somewhat lower rms velocity $u'*$, given in Table 2. Fig. 3 further shows that the fluctuations in

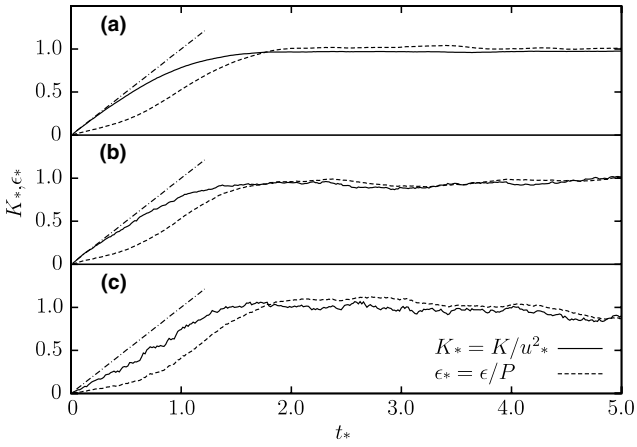

Fig. 3. Time series of kinetic energy and rate of energy dissipation of simulations F_1 (a), F_2 (b) and F_6 (c).

the kinetic energy and the rate of energy dissipation increase for simulations F_2 and F_6. The standard deviation in K (determined from the steady-state part of the time series) for these three simulations was 0.6%, 3.2% and 4.8% respectively.

One phenomenon that can be observed in Fig. 3 is that the evolution of the rate of energy dissipation follows that of the kinetic energy with a time lag. Most kinetic energy is contained at the large scales. The turbulent flow field needs to develop before fluid motion reaches the length scales where dissipation takes place. The increase of the rate of energy dissipation therefore lags the development of the kinetic energy. An approximate time scale for the transfer of kinetic energy [18] is $\frac{1}{10}T_e$ ($T_e = K/\epsilon$, the eddy turnover time-scale). For the cases in Fig. 3, this time is $t* = 0.1$, which to order of magnitude corresponds with the time lag of the energy dissipation.

5.3. Flow field and energy spectra

The energy spectra of Fig. 5(a) show that with a decrease in Kolmogorov length scale (simulations F_3, F_1 and F_4), fluid motion is generated up to higher wave numbers. This is also visible in the flow fields in Fig. 4. The spectra indicate that as the Reynolds number increases, the energy spectrum at higher wave numbers increases and approaches the $-5/3$ slope that is associated with the energy spectrum of the inertial subrange (see Eq. (1)).

In simulation F_4, the Kolmogorov length was much smaller than the rule of thumb minimal value of 0.318 [lu]. The energy spectrum of simulation F_4 demonstrates that the energy content at the smallest scales has risen approximately six orders of magnitude. As a result, the gradients at the small length scales become too steep and although on the large scales the fluid motion still exhibits a consistent energy spectrum, the fluid motion at the smallest scales is not accurately resolved, as can be observed from the spurious behaviour of the velocity vectors in the flow field. Although the simulation remains stable, the flow field of Fig. 4(c) demonstrates that the flow field at the smallest scales becomes physically unrealistic (indicated also by ϵ/P and S_g in Table 2).

The dissipation spectra (Fig. 5(b)) show a shift of energy dissipation towards higher wave numbers when the

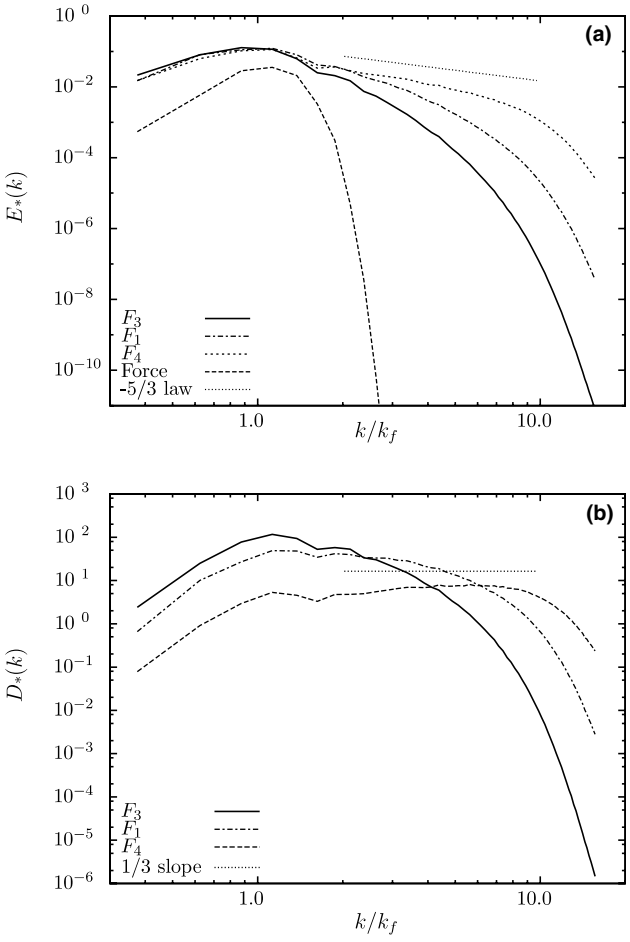

Fig. 5. Normalised energy spectrum (a) and dissipation spectrum (b) for simulations F_3, F_1 and F_4 at increasing order of Reynolds number. ($E*(k) = E(k)/(u*^2 l*)$, $D*(k) = D(k) \times l*^2/u*^3$).

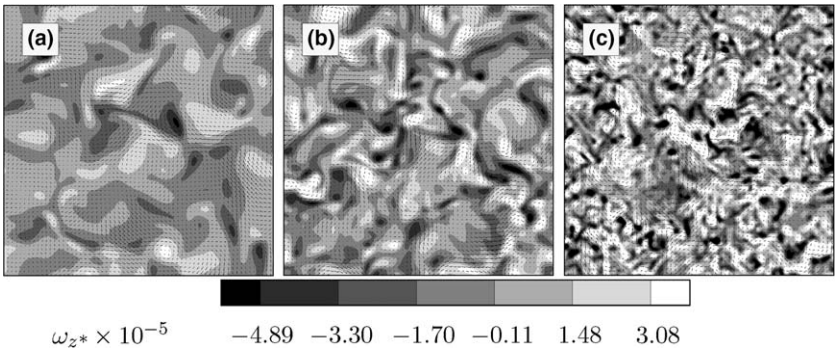

Fig. 4. Cross-section of the flow fields of simulations F_3 (a), F_1 (b) and F_4 (c). The contours indicate the vorticity component ω_z, perpendicular to the plotted plane.

Reynolds number is increased. For simulations F_3, F_1 and F_4, the power input and hence the total energy dissipation is identical. As a consequence, the integrated value of the dissipation spectrum should be equal for these three simulations. For simulation F_3, the dissipation mainly occurs around $k/k_f = 1.0$, whereas for simulation F_4 dissipation extends to $k/k_f = 10.0$. Eq. (33) contains the relation between ϵ, the dissipation spectrum and the energy spectrum, which indicates that the energy is weighted with k^2, which stresses the contribution of the energy spectrum at larger wave numbers in the resulting dissipation spectrum. In the inertial subrange, the dissipation spectrum should obtain a positive slope of $2 - 5/3 = 1/3$, which is indicated in the figure.

The influence of the forcing is clearly visible in the energy and the dissipation spectra. On the one hand, the use of seven Fourier modes for forcing gives an accurate representation of the Gaussian distribution of the forcing intensity (see Eq. (10)) which allows for the use of a large concentration parameter ($f_{nr} = 7,\ c = 1.0$). On the other hand, the effect is that the forcing dominates the energy spectrum and therefore the fluid motion over a larger range of wave numbers. To overcome this behaviour, [1] uses a much smaller concentration parameter ($\mathcal{O}(0.01)$), to concentrate the forcing spectrum around a single wave number k_f. In his results, the energy spectrum therefore exhibits a much narrower peak at its maximum.

By using a larger number of discrete forcing wave numbers and a larger concentration parameter, the power input is distributed more evenly over a wider range of wave numbers. The advantage is that the overall contribution of P_2 will decrease. The value of the fluctuating force $f_\alpha(\mathbf{k})$ will have a lower value at each discrete wave number, and hence the product of $u_\alpha(\mathbf{k})f_\alpha(\mathbf{k})$ will be smaller. If one intends to use the forcing scheme for uncontrolled simulations of turbulence, then in this way the contribution P_2 can be suppressed. However, a disadvantages of this approach is that the energy spectrum is influenced by the forcing scheme over a wide range of wave numbers, rather than being concentrated closely around the forcing wave number k_f. As a result, the reduced range of wave numbers in which the flow field can develop freely will limit the turbulent Reynolds numbers that can be obtained.

Fig. 6 demonstrates the impact of a variation of the number of forced Fourier modes and of a change in k_f on the energy and dissipation spectra. This was tested in simulation F_5. The figure allows a comparison between F_5 and F_1, for which the same forcing Reynolds number was chosen, and between simulations F_5 and F_3, for which the same Kolmogorov length scale was set while F_3 was set at a much lower Reynolds number than the other two cases.

Fig. 6(a) shows that for the scaled energy spectra of F_1 and F_5 practically collapse. Table 2 also indicates that

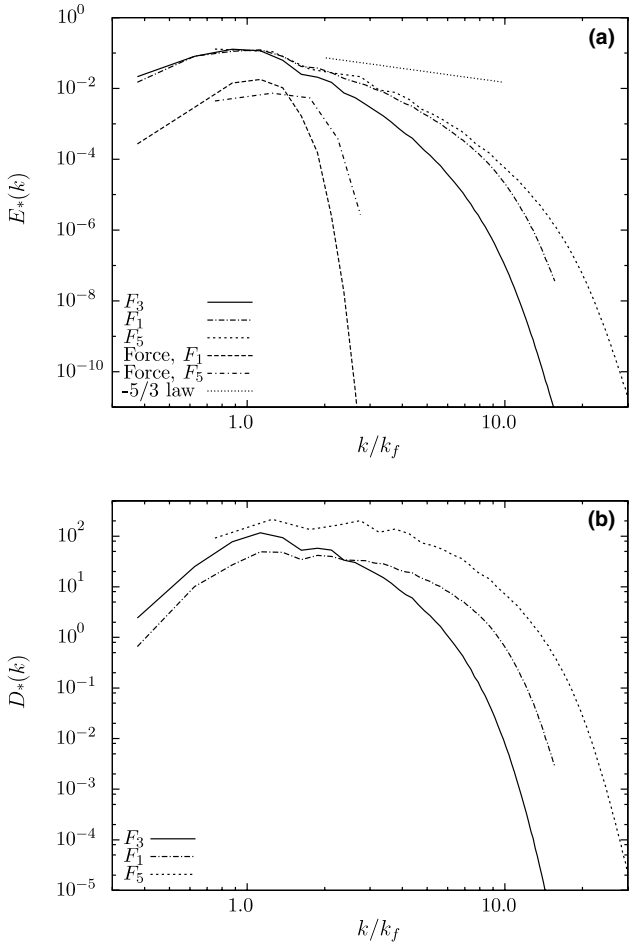

Fig. 6. Normalised energy spectrum (a) and dissipation spectrum (b) for simulations F_3, F_1 and F_5 at order of increasing Reynolds number. ($E*(k) = E(k)/(u*^2 l*)$, $D*(k) = D(k) \times l*^2/u*^3$).

the Taylor Reynolds number of these simulations are of the same order, with F_5 being slightly larger. The energy spectra also show that F_5 lies slightly above F_1. The horizontal axis is scaled with k_f which shifts the energy spectra such that their forcing wave numbers collapse. As a result, for simulations at the same Reynolds number but different values of k_f, their spectra should coincide upon scaling. The figure shows that this is indeed the case.

The flow field of F_5, as well as that of F_3, possessed a higher resolution at the small scales than that of F_1. This is confirmed by the energy and dissipation spectra. The spectrum of F_5 continues up to higher scaled wave numbers than F_1. At the same time, Fig. 6 shows that the energy spectra of F_5 and F_3 continue smoothly up to much lower values of $E*$ and $D*$ than F_1.

Table 2 shows that for F_5, $\epsilon/P > 1.0$. This is due to the poor representation of the Gaussian distribution of $F(k)$ over a limited range of three wave numbers. Due to discretisation, the resulting power input P_1 was considerably larger than the desired power input ($P_1 = 1.154 \times P_{\text{input}}$). This discretisation error was negligible for simulations with $f_{nr} = 7$. An increase of 15% in

power input results only in a 4% decrease in Kolmogorov length since $\eta \sim \epsilon^{-1/4}$ and the turbulent conditions were hardly influenced, as was confirmed by the energy spectra.

5.4. Grid anisotropy and the correlation functions

For simulations F_1 and F_7, the longitudinal and transverse correlation functions, $f(r)$ and $g(r)$ respectively, are given in Fig. 7. The correlation functions give a measure for the velocity correlation over a separation r, parallel or perpendicular to each velocity component;

$$f(r) = \frac{\overline{u_1(\mathbf{x})u_1(\mathbf{x}+r\mathbf{n}_1)}}{u'^2}$$
$$g(r) = \frac{\overline{u_1(\mathbf{x})u_1(\mathbf{x}+r\mathbf{n}_2)}}{u'^2}, \qquad (35)$$

where $\mathbf{n}_\alpha$ indicates the primary axes in direction α.

In Fig. 7(a), these functions are plotted for simulation F_1. Both the longitudinal correlation $f(r)$ and the transverse correlation function $g(r)$ exhibit the well-known behaviour of the spatial correlation functions for turbulent flows. The function $f(r)$ is typically larger and remains positive, while $g(r)$ decays faster to zero and becomes negative. At larger separations both turn to 0, indicating that no self-correlations at the length of the periodic domain occurs.

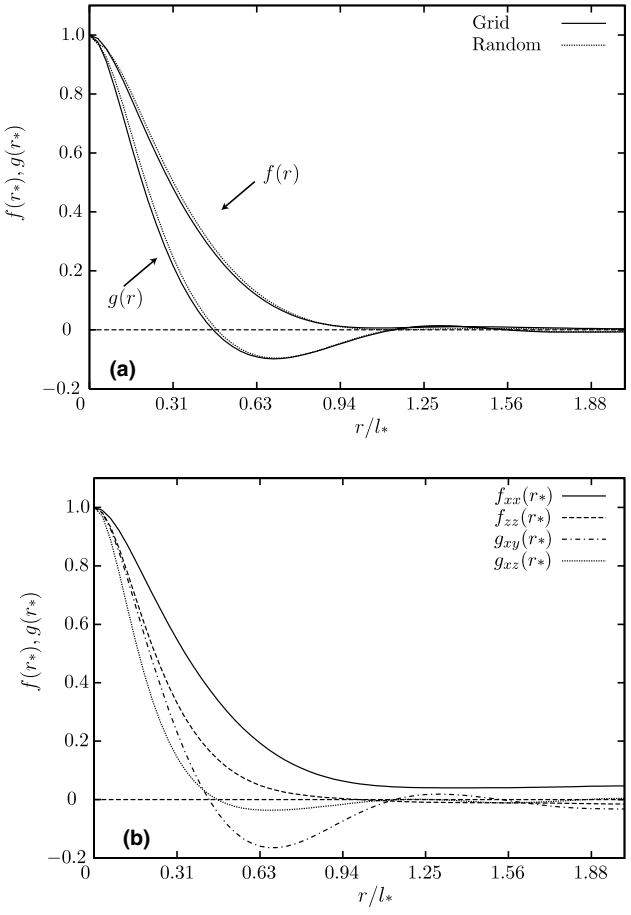

Fig. 7. Normalised autocorrelation functions $f(r)$ and $g(r)$ of (a) simulation F_1, where the correlation functions were determined via the Fourier transform of the velocity field (grid) and via random sample points (random); (b) simulation F_7, where the flow field is anisotropic. The correlation functions were determined from the ensemble average of 15 flow field realisations.

To test if the structure of the computational grid has any consequences for the isotropic properties of the flow field, the correlation functions were determined (i), through the Fourier transform of the velocity field and (ii) through sampling of the flow field via a large number of randomly placed sample points.

When determining the correlation functions via the Fourier transform, the orientation of the velocity field is determined based on the orientation of the computational grid and anisotropic properties that may be present due to the grid are contained in the resulting correlation functions. For the second method, the velocity field was sampled with a large number (100,000 per field) of randomly placed points. The fluid velocity was computed at these points via first order interpolation. The correlation functions were then determined by calculating the correlation between all pairs of sample points. The orientation was based on an internal coordinate system, determined by the axis connecting each pair and two axes that are perpendicular to the connecting axis and to each other. By using random pairs of particles the orientation of the coordinate system is randomised for each pair. For a truly isotropic field and ideal interpolation, both methods should give the same $f(r)$ and $g(r)$. The slightly higher values of the randomly determined correlation functions may be a result of the accuracy of the interpolation procedure. Generally, the good correspondence between the correlation functions obtained via both methods shows that no gross anisotropy is present in the simulations.

The correlation functions presented in Fig. 7(b) give the longitudinal and transverse correlation of the anisotropically forced simulation F_7. In this simulation the anisotropic forcing parameter b was set to a value of 10, indicating that the power input in the x- and y-directions was 11.3 times that of the z-direction. The longitudinal correlation function f_{xx} describes the correlation of the x velocity component over a separation in the x direction while the transverse correlation function g_{xy} presents the correlation of the x velocity component over a separation in the y direction. The figure demonstrates that the f_{zz} correlation decays faster than f_{xx}. The correlation length scale $\Lambda*_f$ gives a measure for the integral length scale over which the correlation drops to zero, comparable to the integral length scale Λ_s*. It is anticipated that $\Lambda*_f$ will be smaller in the z-direction than in the x- or y-direction since the integral length scales with u'^3 and u'_x or u'_y are larger than u'_z. This was confirmed by the values determined for $\Lambda*_{f_{xx}}$ as

0.459 and for $\Lambda*_{f_{zz}}$ as 0.274. It is also observed that f_{xx} does not return to zero. This indicates that due to the enhanced large scales in the x–y plane, self correlation with the periodic mirror image occurs, which is an artifact of the simulations. The figure further shows that the transverse correlation g_{xy} generally has a larger positive value, crosses the function g_{xz} around zero and reaches a lower minimum value than g_{xz}, before returning to zero.

5.5. Axisymmetric anisotropic turbulence

The time-series of the Reynolds stresses $R_{ij}(=\overline{u_i u_j})$ of simulation F_7 (Fig. 8) show the evolution of the anisotropic forced turbulence. At startup, the magnitude of the x and y velocity-components increase much faster than the z-component, as is anticipated since the forcing is 11.3 times larger in the x–y plane. It is clearly demonstrated that momentum transfer from the x–y plane into the z direction occurs once the flow field is sufficiently developed. Although the forcing input is 11.3 times larger in the x–y plane, the ratio of R_{xx} or R_{yy} over R_{zz} becomes roughly 2 in steady-state. At the same time, the off-diagonal components of R_{ij} fluctuate around zero.

The anisotropy of the flow field can be characterised by the anisotropy tensor a_{ij}, defined as

$$a_{ij} = \frac{R_{ij}}{K} - \frac{2}{3}\delta_{ij}, \tag{36}$$

and is characterised by its invariants. The first invariant of this tensor is zero by definition while the second and third invariant are $A_2 = a_{ij}a_{ji}$ and $A_3 = a_{ij}a_{jk}a_{ki}$. For 3D isotropic flow, both invariants are zero. In Fig. 9, the second invariant of the anisotropy tensor is plotted against the third invariant for the whole time series of both simulations F_2 and F_7. Fig. 9(b) gives a detail of figure (a) to demonstrate that in the case of isotropic forcing the invariants are practically zero and bounded by the Lumley triangle [21].

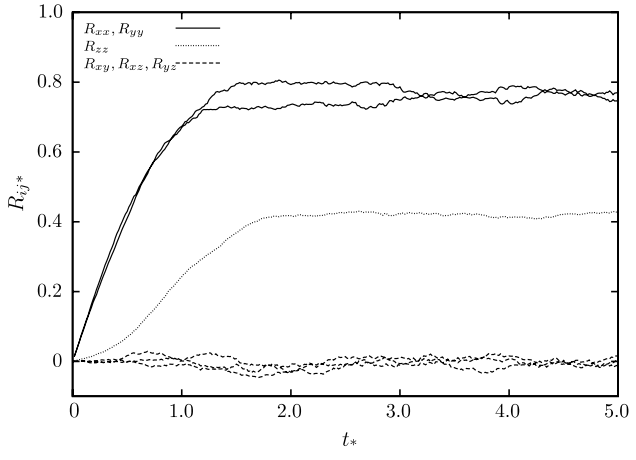

Fig. 8. Time series of the normalised Reynolds stresses of simulation F_7.

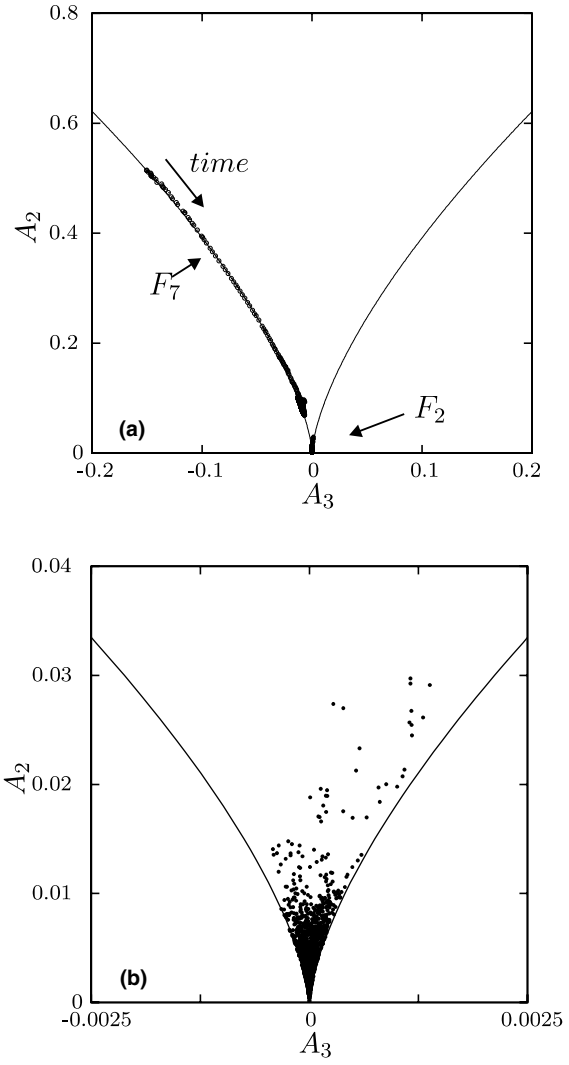

Fig. 9. Invariants A_2 and A_3 calculated from the time series of the Reynolds stresses of simulations F_2 and F_7 (a). The lines indicate the position of the Lumley triangle. F_2 fluctuates close to zero, as indicated in the enlargement (b).

With the choice of the anisotropic forcing presented here, P_x and P_y are equal and much larger than P_z, which results in axisymmetric anisotropic turbulence. For this type of flow, the anisotropy tensor can be written as

$$a_{ij} = \begin{pmatrix} \alpha/2 & 0 & 0 \\ 0 & \alpha/2 & 0 \\ 0 & 0 & -\alpha \end{pmatrix}, \tag{37}$$

and the corresponding invariants can be expressed in terms of the parameter α. For the case where the power input in the symmetry plane exceeds that of the out-of-plane direction it is found that $\alpha > 0$. The relation between the two invariants then becomes $A_3 = -6(A_2/6)^{3/2}$, while $A_3 = 6(A_2/6)^{3/2}$ is valid when the opposite holds, i.e. for $\alpha < 0$.

These two curves are plotted in the A_2–A_3 plane of Fig. 9 and pose a limiting case for anisotropic turbulence. The point where the two lines cross represents the bottom corner of the so-called Lumley triangle (see [21] or [22]). Fig. 9(b) demonstrates that the invariants of the isotropic simulation F_2 are indeed bounded by the two branches of the Lumley triangle and are close to zero, indicating isotropic turbulence.

With R_{zz} being smaller than R_{xx} or R_{yy} for simulation F_7, $\alpha > 0$ and the points in the A_2–A_3 plane are accordingly found near or at the left branch of the Lumley triangle. This demonstrates that axisymmetric turbulence is obtained throughout the time series of the simulation. The time average steady-state value of α was 0.237. The dots near the left line show the evolution of the anisotropy in the A_2–A_3 plane. As already noticed, from start-up of the simulation R_{zz} lags the steep increase of R_{xx} and R_{yy}. Consequently, the invariant A_3 starts at an initial value of -0.15 and proceeds in time to a steady-state value of approximately -0.01.

5.6. Numerical performance

The numerical performance of the simulations was tested on a parallel platform that consisted of dual Intel Xeon CPU's operating at 3.4 GHz that was equipped with a TopSpin InfiniBand network for fast parallel computing. The Intel Fortran and C compilers were used for compilation of the FFTW and lattice-Boltzmann codes.

The simulation time for 1000 time steps was taken as a measure for the overall performance of the simulations and included start-up and data io for writing datafiles. Only multi-processor simulations were tested. The total simulation time of simulation F_1, running on two CPU's of one node, was 6520 s. The simulation time for F_2, the case of uncontrolled forcing, was 3910 s. This difference in simulation time demonstrates the considerable contribution of the Fourier transform to the computational effort.

The speed-up of simulations F_1 and F_2 are compared in Fig. 10. The simulation time of case F_1 on two CPU's, $T_{F_{1,0}}$, was chosen as the basis for comparison. As performance index, the ratio of computational times $2T_{F_{1,0}}/T$ was chosen. This ratio is multiplied by a factor two to indicate that case $F_{1,0}$ was computed on two CPU's and therefore nominally runs two times faster than a simulation on one CPU. T is the computational time of simulations F_1 and F_2 at increasing number of CPU's.

The filled dots in Fig. 10 indicate the performance of simulation F_1 when the number of CPU's is increased from 2 to 16. The drawn line indicates ideal speed-up, indicating a two times faster simulation for a double number of CPU's. The speed-up of case F_1 stays below this line. At 16 CPU's the speed-up reaches 90% of the ideal speed-up. With a 100% speed-up at 8 CPU's and a small decrease to 97% at 16 CPU's, the performance of case F_2, open symbols, is much closer to ideal.

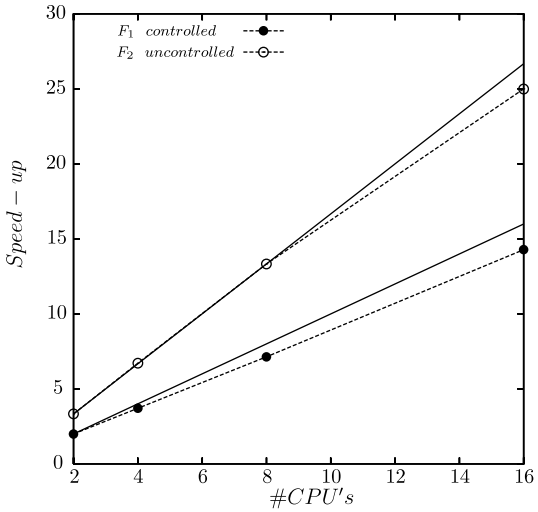

Fig. 10. Speed-up of simulations F_1 and F_2 when increasing from 2 to 16 CPU's.

The decreasing performance at increasing number of CPU's is caused by the increasing need for communication. The fast Fourier transform requires an all-to-all communication between all CPU's and therefore the slope of the speed-up of case F_1 is clearly lower than 1. At increasing number of CPU's the slab-wise domain decomposition also starts to have an impact on the efficiency of the lattice-Boltzmann scheme. While this scheme requires a minimal amount of communication relative to the number of operations per CPU, with larger number of CPU's, the ratio of communication to computation increases. Nevertheless, a speed-up of 90% or more at 16 CPU's can be considered very efficient.

6. Conclusion

In this paper, it has been demonstrated that the forcing scheme for the generation of sustained homogeneous turbulent conditions, as proposed by Alvelius [1], could be successfully combined with a lattice-Boltzmann scheme. With this forcing scheme, a turbulent flow field can be obtained with a priori defined turbulent properties. It has been demonstrated that by straightforward implementation of this spectral forcing scheme in the lattice-Boltzmann framework the specific features of suppression of force–velocity correlation and anisotropic forcing are recovered. A possible minus compared to other numerical schemes could be the relatively large memory requirements for the lattice-Boltzmann scheme, which requires up to 19 floats per grid point. An advantage of the combination of spectral forcing with the lattice-Boltzmann scheme is the good scalability on parallel

computer platforms that is retained with the spectral forcing scheme. The lattice-Boltzmann scheme proves to be an accurate and stable method for direct numerical simulation of turbulence.

References

[1] Alvelius K. Random forcing of three-dimensional homogeneous turbulence. Phys Fluids 1999;11(7):1880–9.

[2] Tennekes H, Lumley J. A First Course in Turbulence. 2nd ed. The MIT Press; 1973.

[3] Smagorinsky J. General circulation experiments with the primitive equations. 1: The basic experiment. Mon Weather Rev 1963;91: 99–164.

[4] Lesieur M, Metais O. New trends in large-eddy simulation of turbulence. Annu Rev Fluid Mech 1996;28:45–82.

[5] Eswaran V, Pope SB. An examination of forcing in direct numerical simulations of turbulence. Comput Fluids 1988;16(3): 257–78.

[6] Overholt M, Pope SB. A deterministic forcing scheme for direct numerical simulations of turbulence. Comput Fluids 1998;27(1): 11–28.

[7] Chopard B, Droz M. Cellular automata modeling of physical systems. 1st ed. Cambridge, England: Cambridge University Press; 1998.

[8] Succi S. The lattice Boltzmann equation for fluid dynamics and beyond. 1st ed. Oxford University Press; 2001.

[9] Chen S, Doolen G. Lattice Boltzmann method for fluid flows. Annu Rev Fluid Mech 1998;30:329–64.

[10] Rothman DH, Zaleski S. Lattice-gas cellular automata. 1st ed. Cambridge University Press; 1997.

[11] Eggels JGM, Somers J. Numerical simulation of free convective flow using the lattice-Boltzmann scheme. Int J Heat Fluid Flow 1995;16:357–64.

[12] Bhatnagar B, Gross E, Krook M. A model for collision processes in gases. i: small amplitude processes in charged and neutral one-component system. Phys Rev 1954;94:511–25.

[13] Qian Y, d'Humieres D, Lallemand P. Lattice bgk models for Navier–Stokes equation. Euro Phys Lett 1992;17(6):479–84.

[14] Guo Z, Zheng C, Shi B. Discrete lattice effects on the forcing term in the lattice Boltzmann method. Phys Rev E 2002;65(4):046308.

[15] Somers J. Direct simulation of fluid flow with cellular automata and the lattice-Boltzmann equation. Appl Sci Res 1993;51:127–33.

[16] Frigo M, Johnson SG. Fftw 2.1.5. Available from: www.fftw.org.

[17] Moin P, Mahesh K. Direct numerical simulation: a tool in turbulence research. Annu Rev Fluid Mech 1998;30:539–78.

[18] Pope SB. Turbulent flows. 1st ed. Cambridge University Press; 2000.

[19] Hinze J. Turbulence. 2nd ed. New York: McGraw Hill; 1975.

[20] Wang L-P, Wexler AS, Zhou Y. Statistical mechanical description and modelling of turbulent collision of inertial particles. J Fluid Mech 2000;415:117–53.

[21] Lumley J. Computational modeling of turbulent flows. Adv Appl Mech 1978;24:123–76.

[22] Derksen J, Doelman M, Van den Akker HEA. Three-dimensional lda measurements in the impeller region in a turbulently stirred tank. Exp Fluids 1999;27:522–32.